Terawatt-laser-driven electron bunch with energies up to 25 MeV using robust fast self-replenishing liquid jet target

K. A. Ivanov,[1,2] S. A. Shulyapov,[1] D. A. Gorlova,[1] I. P. Tsygvintsev,[3] I. N. Tsymbalov,[1,4] A. Yu. Zavorotny,[1] R. V. Volkov,[1] and A. B. Savel'ev[1,2]

[1]*Physics Faculty of M.V. Lomonosov Moscow State University, 119991, Moscow, Russia*
[2]*Lebedev Physical Institute of the Russian Academy of Sciences, 119991, Moscow, Russia*
[3]*Keldysh Institute of Applied Mathematics of the Russian Academy of Sciences, 125047, Moscow, Russia*
[4]*Institute for Nuclear Research of the Russian Academy of Sciences, 117312, Moscow, Russia*

(Received 29 October 2025; accepted 4 May 2026; published 29 June 2026)

A repetitive source of collimated, high-energy electrons is experimentally demonstrated using a 1.3 TW femtosecond laser pulse. The source is based on the efficient coupling of the pulse with an undercritical plasma slab formed by a nanosecond prepulse-induced breakdown of a thin liquid ethanol microjet. By optimizing the temporal delay between the prepulse and the main pulse, a quasi-Maxwellian electron beam is generated with a divergence below 0.1 rad, a detected energy of ~25 MeV, and a charge up to 0.25 nC (3.8 nC/J) in the > 1 MeV range. Numerical simulations corroborate the experimental results and point to a complex acceleration mechanism involving direct laser acceleration and self-modulated laser wakefield acceleration within a bell-shaped plasma profile. This versatile approach highlights the particular advantages of liquid targets, including robustness, simplicity, and suitability for long-term operation in vacuum, for future high-repetition-rate laser-plasma applications.

DOI: 10.1103/ccf6-tyr4

I. INTRODUCTION

Since the proposals for laser-driven electron beam generation in undercritical plasma, based on laser wakefield acceleration (LWFA) by plasma fields [1] or direct laser acceleration (DLA) by the laser field in the plasma channel [2], many efforts were directed toward reaching ultimate electron beam parameters (both charge and energy) with the utilization of up-to-date laser technologies [3–5]. Today, with petawatt-class lasers, one can generate highly collimated electron beams with energies up to 10 GeV via the LWFA approach [6] and μC charge electron beams with energies of tens of MeV in the DLA concept [7], forming a laser-driven source delivering extreme peak power, which finds prospective applications [8,9]. However, the implementation of these schemes with modest terawatt-class laser systems sets limitations on the acceleration efficiency caused by depletion of the laser pulse, as well as suppressed laser to plasma coupling because of lower peak intensity. At the same time, the ability to efficiently convert laser energy into electron beams with relatively low-power lasers is of key importance given the high repetition rates available (up to kHz) [10,11], allowing a substantial increase in both the peak and average power of the laser-plasma source. To a large extent, success hinges on optimizing targetry and plasma parameters to (i) trap a large number of electrons and (ii) drive energy gain for high longitudinal momentum with low divergence. Various approaches have been considered with gas targets, such as plasma profiling with downramps and shocks [12,13], adding high-Z gas to the mixture for ionization injection [14,15]. Operation in an initially denser plasma medium is also feasible with ultrashort almost single-cycle pulses [16] or in the self-modulated regime (SM-LWFA) [17] for mismatched plasma and pulse duration. However, enhanced charge with broadened a quasi-Maxwellian spectrum may be obtained in the transition to DLA closer to the critical plasma density [18,19]. Complex interplay of the DLA and LWFA mechanisms was also reported [20,21].

Efficient electron injection and trapping as well as self-focusing conditions could be fulfilled in gas-cluster mixtures [22,23]. For terawatt lasers, this type of target provides nC/J divergent electron beams with energy up to tens of MeV [22–25]. Operating at a high repetition rate strongly complicates the use of gas jets because of the extreme load onto the pumping system. From this point of view, the transition to fully overdense targets with a high surface refresh rate could be a promising solution. Electron beams at up to 1 kHz were recently demonstrated from the front surface plasma of a metal [26], plastic [4], quartz [27],

Published by the American Physical Society under the terms of the Creative Commons Attribution 4.0 International license. Further distribution of this work must maintain attribution to the author(s) and the published article's title, journal citation, and DOI.

liquid stream [28], and droplet [29]. For a thin solid or liquid target, the prepulse could form an extended plasma slab with undercritical density for efficient electron beam generation in the forward direction [30–32]. A liquid target is supposed to be promising due to fast self-replenishing and low debris.

In this paper, we report the generation of a low-divergence (<0.1 rad) electron beam with a quasi-Maxwellian spectrum, maximal energy ∼25 MeV, and charge up to 3.8 nC/J for electrons >1 MeV using a 1.3 TW femtosecond laser pulse at 10 Hz repetition rate. The acceleration occurs in the undercritical plasma formed by the breakdown of a 40 μm cylindrical continuous liquid ethanol jet, with the prospect of scaling the repetition rate up to the kHz level, opening a novel route for a simple design and a brilliant laser-driven source. Numerical simulations, being in good agreement with experimental results, shed light on the energy gain mechanism.

II. EXPERIMENTAL PARAMETERS

The liquid ethanol cylindrical vertical jet with a flow velocity of 10 m/s was generated by a microcapillary with a 40 μm orifice (MicroFab MJ-AB-01-40) and had a liquid consumption below 1mL/min. A three-dimensional motorized stage was utilized to adjust the jet position with 2.5 μm accuracy. A nanosecond Nd:YAG laser pulse (hereinafter NSP), with an 8 ns full width at half maximum (FWHM), intensity $\sim 8 \times 10^{12}$ W/cm^2, 1064 nm wavelength, and 0.5 ns temporal jitter, irradiated the jet surface after being focused by an off-axis parabola, forming a hydrodynamically expanding plasma slab [30]. The 1.3 TW femtosecond pulse (FSP) was focused by the same parabola into a 3.2 ± 0.2 μm FWHM spot to a vacuum peak intensity $I = 8 \times 10^{18}$ W/cm^2 (805 nm, 50 fs, 65 mJ on target, $M^2 = 1.9$). The amplified spontaneous emission pedestal of the pulse was evaluated at a level of 2×10^{-7} in the time window from 100 to 10 ps prior to the main pulse. The FSP pulse passed with a controlled delay τ relative to the peak of the nanosecond pulse with an accuracy of 250 ps in the range from −10 to +10 ns (positive value corresponds to the case when the peak of the NSP pulse precedes the FSP pulse). Hence, the maximum plasma density of the slab was determined by this delay. Coincidence of the foci in the transverse plane was monitored by a microobjective and adjusted by a precise angular mount of the NSP radiation mirror. A split-off portion of the FSP radiation at the doubled frequency formed a shadowgraphic channel, revealing the NSP-pulse-induced plasma evolution in the forward direction. The spatial stability of the jet is below 5 μm at distances up to 10 mm below the orifice, which allows one to irradiate the target without damaging the capillary. On the one hand, this positively distinguishes our approach from gas jets being subject to destruction [33]. On the other hand, debris from the pure ethanol jet evaporates quickly in vacuum and does not necessitate protecting optics unlike for solid targets (tapes, wires, plates). Simple collection of the liquid in a reservoir with a differential pump ensured overall robust design and allowed us to operate in a forepumped vacuum chamber with residual pressure $(3–5) \times 10^{-2}$ mbar. A closed loop liquid recirculation may be added with a peristaltic pump [34]. A sketch of the experimental setup is presented in Fig. 1.

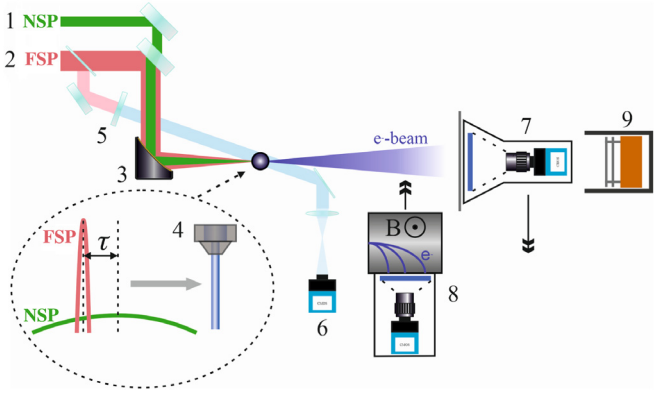


FIG. 1. Graphical representation of the experimental setup: nanosecond laser pulse, NSP (1); femtosecond laser pulse, FSP (2); off-axis parabolic mirror (3); liquid ethanol jet (4); second harmonic crystal for the shadowgraphic imaging channel (5); shadowgram imaging camera (6); scintillation Lanex screen for electron beam visualizer with camera (7); single-shot electron beam energy spectrometer (8); and Faraday cup charge detector (9).

The electron beam was detected in the forward direction on a Lanex scintillating screen imaged on a CMOS camera. The detector was shielded by a 1 mm Pb plate to prevent electrons below ∼2 MeV from reaching the screen. The spectrum of the electron beam was measured by an energy-calibrated, single-shot magnetic spectrometer with a resolution $dE/E < 0.2$ and visualization on a scintillation screen, which could be introduced in front of the Lanex beam visualizer. The volume between the spectrometer magnets was $2.8 \times 10 \times 5$ cm^3 and the maximum magnetic field was 0.56 T. To evaluate the charge, a Faraday cup with acceptance angle 0.17 rad could be installed into the beam path with two aluminum electrodes catching electrons above roughly 0.05 and 1 MeV. Cross-check measurements were conducted by the photonuclear technique supported by the GEANT4 modeling [35]. This method is based on the detection of photoneutrons in the disintegration reactions in Be and W catchers by the electron bunch (accounting for bremsstrahlung gammas in a high-Z converter).

III. RESULTS AND DISCUSSION

A. Experimental data

Figure 2(a) illustrates the integrated luminosity Q (proportional to the beam charge above 2 MeV) of the Lanex versus the delay τ between NSP and FSP pulses, with a well-defined extremum near $\tau = 2$ ns (considering

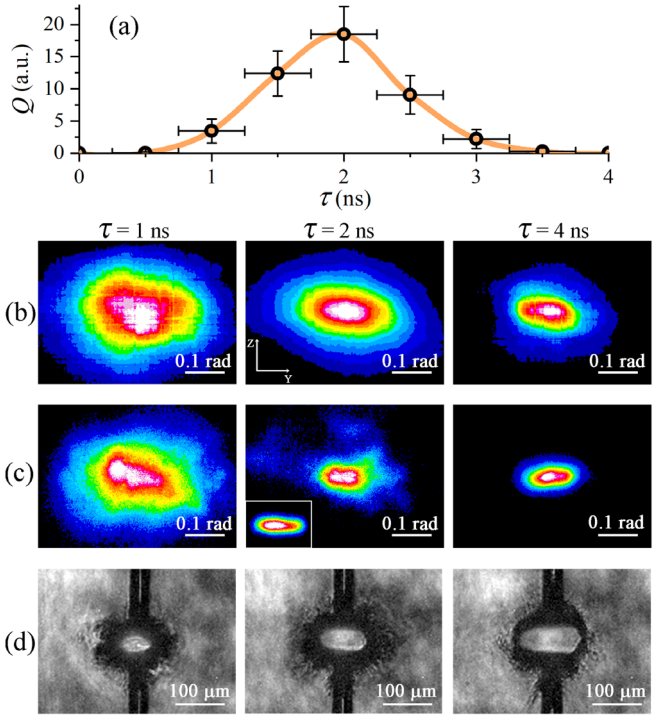


FIG. 2. Integrated Lanex luminosity versus the delay τ (a). Averaged over series of shots (b) and typical single shot (c) beam imprints at varied τ for electrons above 2 MeV. Inset in image for $\tau = 2$ ns represents the imprint of electrons with energy > 4 MeV. Frontal shadowgrams of the liquid jet affected by the NSP pulse at varied τ (d).

temporal jitter of the NSP pulse), indicating a strong correlation of the acceleration efficiency with the plasma slab profile. As seen in Fig. 2(b), transition occurs from a divergent (>200 mrad) beam at $\tau = 1$ ns, typical for the limited acceleration length in a relatively dense plasma (DLA), to a well-collimated bunch (~50 mrad) of electrons with a small charge ($\tau = 4$ ns), accelerated rather by the longitudinal plasma waves. A complex interplay of these effects is observed at intermediate delays ($\tau = 2 \pm 0.25$ ns), when the bunch reaches maximal charge with restrained angular spread (< 0.1 rad). Nevertheless, the ellipticity of the imprints (oblong beam along the horizontal axis Y that coincides with the laser polarization) supports our assumption that the DLA stage is essential at any delay. It is worth mentioning that the maximal flux of electrons was detected with the waist position of the FSP pulse ~20 μm above the jet surface before the NSP pulse irradiation (note the estimated Rayleigh length of 15 μm). When focusing the moderate power laser pulse closer to the jet initial surface (i.e., the waist being in denser plasma), the counterplay of ionization defocusing before the focal area hampers the development of the relativistic channel. The NSP pulse Rayleigh length is much larger (over 100 μm).

Typical single shot imprints of the above 2 MeV electron beams at varied τ, Fig. 2(c), follow the averaged images. However, a lower divergence was noticed for electrons with energy >4 MeV (detected by adding another 1 mm Pb plate in front of Lanex), as seen in the inset in the image at $\tau = 2$ ns. Hence higher momentum is gained in the longitudinal direction. The divergence of high-energy electrons (>4 MeV) in the plane of polarization Y and perpendicular to it Z is 80 ± 20 and 40 ± 12 mrad, respectively, at the optimal delay $\tau = 2$ ns.

One should note that, according to the frontal shadowgrams, see Fig. 2(d), the area of the jet breakdown is characterized by an undercritical density plasma (transparent for the backlighting 400 nm radiation) with gradually increasing hole dimensions. The latter is elliptical (~90×50 μm at $\tau = 2$ ns), with the larger dimension perpendicular to the jet axis (due to the absence of liquid matter unlike in the vertical direction). Spectral measurements revealed that the energy distribution of the bunch is quasi-Maxwellian at $\tau = 2$ ns, see Fig. 3(a), with a slope of $T = 5.9 \pm 1.5$ MeV (~$\exp(-E/T)$ fit in the high-energy range) and the maximum detected energy exceeding 25 MeV. The orange stripe depicts variations of the spectrum within a series of shots. The evaluated with Faraday cup average charge of the bunch within a few hundred consecutive shots is 0.15 ± 0.07 nC for electrons above 1 MeV at $\tau = 2$ ns. Approximately 15% of shots yielded charges above 0.18 nC, with a maximum value of 0.25 nC (or 3.8 nC/J of laser pulse energy). The charge is above 0.5 nC (or 7.7 nC/J) in the range >50 keV (this is the lower estimate taking into consideration the detector acceptance angle). Photonuclear measurements with Be and W catchers and posterior modeling based on the known

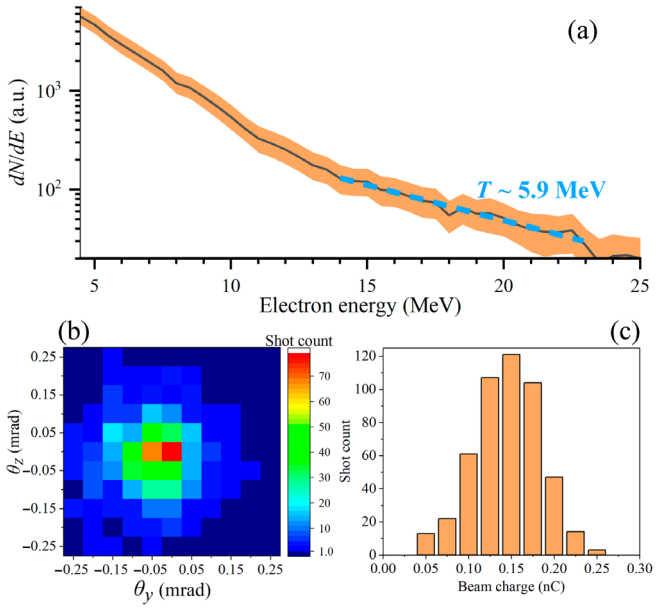


FIG. 3. Spectrum of the electron bunch (a), orange strip is the uncertainty. 2D histogram of angular stability of the center of mass of the bunch (b). Distribution of the bunch charge in series of shots (c).

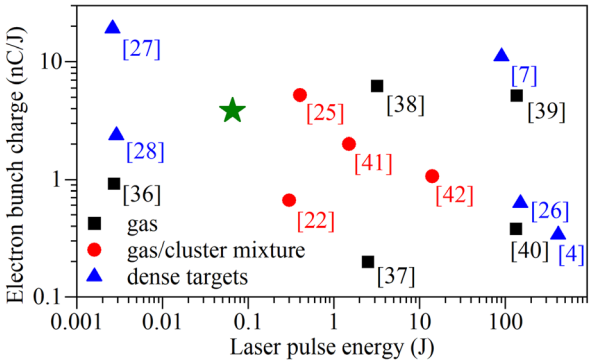


FIG. 4. Plot of the electron beam charge from laser-plasma accelerators with different types of targets. Our result with charge 3.8 nC/J above 1 MeV is presented as the green star.

spectrum [35] support well with the data and provide similar values of ∼0.27 and ∼0.2 nC above 1 MeV in 10% of the shots. 2D histogram of the center of mass of the beam on Lanex (Y, Z) plane in a continuous series of shots and the histogram of bunch charge are presented in Figs. 3(b) and 3(c). The estimated charge substantially surpasses our previous observations at the lower peak power of the FSP pulse (1 TW) [30,32]. We suppose that the acceleration efficiency could be further enhanced with a slight intensity growth.

This bunch charge is among the highest previously published when normalized to 1 J of laser energy. In Fig. 4, we compared a set of examples reported by other groups. Corresponding papers are listed in Table I. We emphasize that this graph is not a ranking table, since different groups report, first, different beam divergence and, second, make measurements with various minimum energy thresholds. One should note that most of the experiments were carried out with gas or gas/cluster targets. Electron bunches from plasma of relatively dense targets are marked by blue triangles (1—SiO_2 disk [27], 2—liquid jet [28], 3—low density foam [7], 4—Cu plate [26], 5—CH foil [4]). Although it remains below the performance achieved with well-optimized foam targets in the single-shot regime, our approach, in addition to its notable acceleration efficiency, stands out for its high average current together with the simplicity and robustness of its experimental implementation. One should also note that in the study employing a rotating-disk target (blue triangle [27] in Fig. 3), the charge was integrated over a wide angular range for electrons with energies above 150 keV.

TABLE I. Additional notes on the data in Fig. 4.

	References	Target material	Reported beam charge, nC/J	Repetition rate, Hz
Gas targets	[36]	H_2	1	1000
	[37]	He	0.2	NA
	[38]	N_2	6.25	0.025
	[39]	He	5.2	Single shot
	[40]	He	0.38	NA
Gas/cluster	[22]	Ar	0.67	10
	[25]	Ar	5.2	10
	[41]	Ar	2	10
	[42]	Ar	1.1	NA
Dense targets	[27]	SiO_2	19.2	1000
	[28]	Water	2.4	100
	[7]	Polymer foam	11.1	Single shot
	[26]	Cu	0.63	Single shot
	[4]	CH foil	0.34	Single shot

It is worth noting that the pure ethanol does not hamper optics reflectivity near the interaction area. After multiple hours of operation, no visible contamination was observed, which is due to the fast evaporation of ethanol. The jet target surface is self-replenished very fast due to continuous liquid flow. The energy deposition of the NSP pulse results in removal of a cylinder of matter a few hundreds of micrometers long from the continuous jet. Considering the jet velocity ∼10 m/s, the consecutive pair of laser pulses (NSPand FSP) could be separated by a millisecond level temporal lag or even less. Hence the repetition rate without updating the targetry could be increased to kHz level.

B. Numerical simulations

In support of experimental findings, a two-stage modeling was carried out. In the first step, a 3D hydrodynamic simulation was performed using the 3DLINE code [43], in which a column of ethanol (initial density 0.79 g/cm^3 and temperature 300 K) was irradiated by the NSP pulse, with parameters similar to the experimental ones. Due to the symmetry, the calculation was performed in 1/4 of the total volume with mirror boundary conditions at $Y = 0$ and $Z = 0$ on a regular cubic grid of 0.5 μm. The calculation domain size was 200 μm along the laser axis and 60×60 μm in the orthogonal plane (i.e., $400 \times 120 \times 120$ cells and $200 \times 120 \times 120$ μm effective calculation volume). The convergence of the calculation with respect to the grid size was verified and confirmed experimentally at lower laser intensities using general parameters determining the evolution of the target shape (burn time, hole expansion rate, central deflection dynamics). The equation of state was calculated using the Thomas-Fermi model in the FEOS code [44] with semiempirical corrections in the phase transition region (reference point at 300 K, soft sphere model parameters $m = 0.5$, $n = 2.0$).

The local ionization multiplicity was determined from the stationary distribution obtained in the framework of collisional-radiative equilibrium using the THERMOS code [45]. The simulated distribution of the total atomic density N_a (including C, O, and H) in the plane of the laser axis and the jet (X, Z) and in the perpendicular plane (Y, Z) at $X = 35$ μm is shown in Figs. 5(a) and 5(b) ($X = 0$ μm

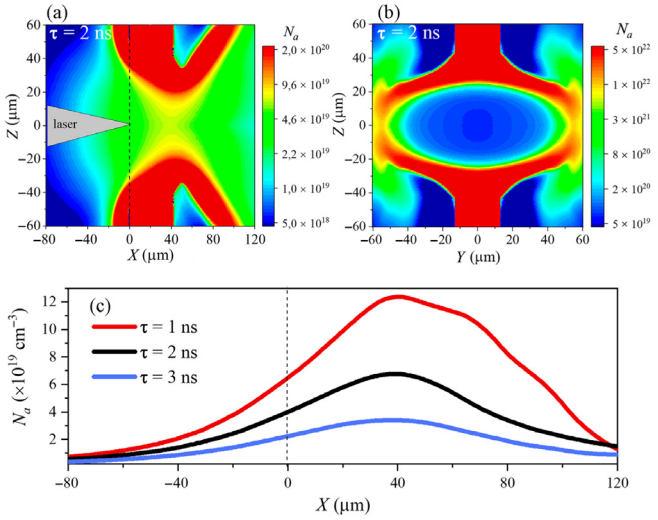


FIG. 5. Simulated atomic density N_a distribution in the area of the jet irradiated by the NSP pulse at $\tau = 2$ ns along the laser axis X (a) and perpendicular to it (b). Axial density profile along the laser direction for different τ (c). Dashed vertical line in (a) and (c) marks the boundary of the jet before irradiation by the NSP pulse.

corresponds to the initial boundary of the jet). The simulation reveals the formation of a low-density plasma-filled hole in the jet with a bell-shaped profile along the laser axis in the region of interaction. The latter is formed already at the peak of the NSP pulse (at $\tau = 0$ ns) by the high-temperature plasma pressure at the front (irradiated) surface of the cylindrical jet. Notice the good coincidence of the breakdown dimensions in the model and experiment, indicating the consistency of the calculations. Fast dynamics of the axial profile of atomic concentration in the area of breakdown is observed, see Fig. 5(c): within 2 ns, N_a decreases from 12 to 3.5×10^{19} cm^{-3} at the peak. Also, the longitudinal profile is subject to rapid evolution. Returning to the experimental data on fast electron beam detected on the Lanex screen in Fig. 2(a), the optimal plasma parameters for efficient electrons acceleration are indeed reached in a narrow temporal range.

Calculated atomic density distributions were then utilized as initial target parameters for 3D3V PIC simulations in the SMILEI code with ionization included [46]. To save computational resources, the modeling was performed in a moving frame X, Y, Z $80\lambda \times 24\lambda \times 24\lambda$ with spatial resolution $dX = \lambda/32$, $dY = dZ = \lambda/4$ ($\lambda = 800$ nm) and temporal step $dt = 0.083$ fs. Initially, the target consisted of H^+, O^{6+} ions, and neutral carbon, with compensating background electrons with density $n_e = N_a \times (0 \times 2/9 + 1 \times 6/9 + 6 \times 1/9)$, considering the ethanol formula C_2H_5OH. The 50 fs FWHM laser pulse was focused to a 4λ spot with maximal normalized field amplitude $a_0 = 0.85\sqrt{I(10^{18}\ \mathrm{W/cm^2})\lambda(\mu\mathrm{m})^2} = 1.9$. The beam waist was placed 20 μm above the unaltered target surface as in the experiment.

According to the simulations, the laser pulse hitting the ascending density part of plasma gives rise to plasma waves induced by backward Raman scattering [observed as rippling of plasma density in Fig. 6(a)], followed by self-focusing near the maximal plasma concentration [31]. The peak amplitude of laser field expressed in units of magnetic field normalized to the vector potential B_z/a_0 rises from 1.9 (vacuum peak intensity) to over 3. Breaking of the plasma wave and ionization of carbon and oxygen inner shells in the high strength field provide seed electrons, which are trapped and then accelerated by the laser pulse in the subsequent DLA stage in the channel near the area with maximal electron density $n_e = 0.1 n_{\mathrm{cr}}$ after ionization, see Fig. 6(a), where n_{cr} is the critical density for the wavelength $\lambda = 800$ nm. The equation $d(\gamma m_e c^2)/dt = -eE_\perp \cdot v_\perp - eE_{||} \cdot v_{||}$ shows that the change in the electron's total energy is due either to the work $W_{y,z} \propto \int E_\perp \cdot v_\perp dt$ done by the transverse electric field of the electromagnetic wave (associated with DLA) or to the work $W_x \propto \int E_{||} \cdot v_{||} dt$ done by the longitudinal electric field of the plasma wave (associated with SM-LWFA) [47]. The role of the transverse field in the electron energy gain at this stage is supported by the analysis of the works of the fields $W_{y,z}$ exerted on the electrons forming the bunch, see diagram in Fig. 6(c). Propagation into the tail part of plasma is accompanied by the self-modulation and formation of subpulses driving longitudinal plasma wave observed in Fig. 6(b), also contributing to the energy enhancement of electrons, see the nonzero work of the longitudinal field W_x in Fig. 6(d). The radial component of the plasma field suppresses the transverse momentum of electrons, producing a lensing effect that results in an electron beam with a divergence below 100 mrad, as shown in Fig. 6(e). At the same time electrons are no longer in resonant conditions for acceleration in the DLA stage, the dephasing leads to energy losses (negative values of $W_{y,z}$ for some electrons). From this point of view, the appropriate termination of this stage is important for high conversion into energetic electrons [48]. Note also the ellipticity of the bunch arising from the DLA stage, see Fig. 6(e), where electrons oscillate along the polarization plane. A similar picture was observed in the experiment, see Fig. 2(c) for $\tau = 2$ ns. The estimated charge is 0.21 nC above 1 MeV in an exponential spectrum with temperature 5 MeV, Fig. 6(f). Charge is lower at other delays as well as the maximal energy of electrons, see other spectra in the same graph. This stresses the role of fine tuning of the experimental parameters to get optimal plasma slab for maximizing the electron bunch energy and charge operating with a moderate peak power laser pulse. Propagation through a dense plasma, typical for $\tau \lesssim 1$ ns, is characterized by trapping a larger number of electrons at the injection stage. However, quick depletion of the laser pulse

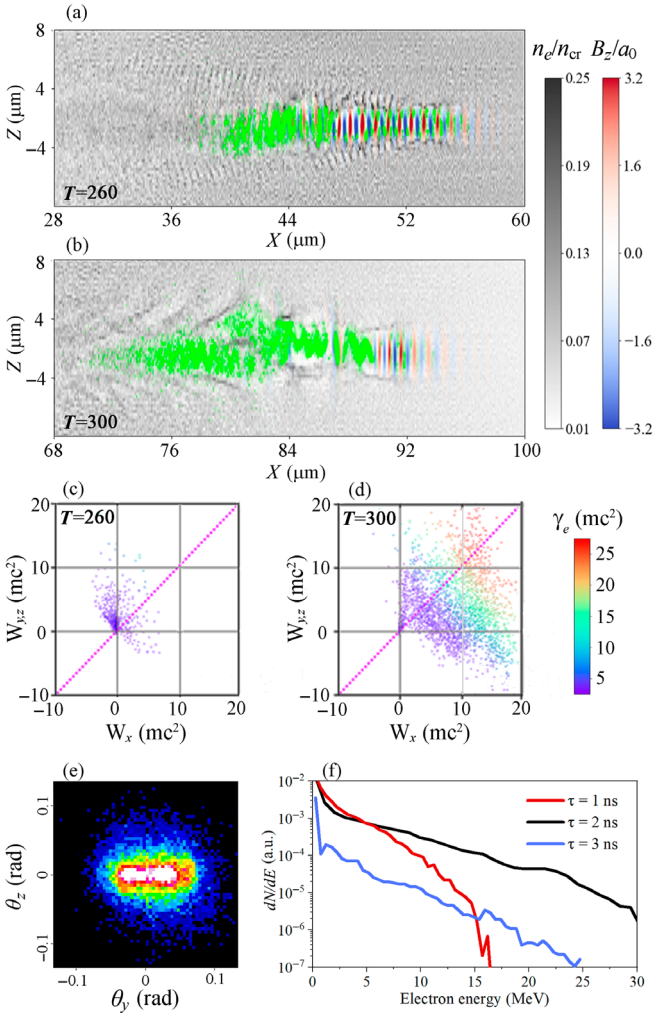


FIG. 6. Electron density n_e distributions and magnetic field B_z amplitude in the simulation box at different simulation periods (a),(b). The axes are calibrated to match the scaling in Figs. 5(a) and 5(c). The green dots mark the electrons with energy >2 MeV at the end of simulations. Works of the longitudinal W_x and transverse $W_{y,z}$ fields at the same simulation periods. Color of the dots corresponds to the electrons γ-factor in units of mc^2. Electron bunch angular distribution (e) at the exit of plasma slab. Electron energy spectra obtained at different delays τ (f).

energy limits the maximal energy of electrons. Plasma rarefication and extension for $\tau \geq 3$ ns does not allow one to trap electrons efficiently, despite the good collimation of the beam and still high maximal energy at the LWFA stage.

The physical principles of the energy gain mechanism are very similar to those observed earlier with a tape target and a liquid jet of larger diameter with lower vacuum peak laser field amplitude $a_0 = 1.5$ [30,31]. However, the slightly enhanced peak intensity in the current modeling $(a_0 = 1.9 \text{ versus } 1.5)$ strongly increased the maximal energy, electron bunch spectral temperature, and charge, as also observed in the experimentally. We suppose that this acceleration mechanism is versatile and basically may be realized with a wide variety of thin targets, made of different materials, where a bell-shaped plasma ramp after ionization and ablation may be obtained.

IV. CONCLUSIONS

In summary, a bright laser-driven source of collimated high-energy electrons was demonstrated with the efficient coupling of a 1.3 TW peak power laser pulse with an undercritical plasma slab. The latter was formed in the area of nanosecond prepulse-induced piercing of a thin (40 μm) liquid pure ethanol cylindrical jet possessing a fast surface refresh rate for operation at high repetition rate without the need of optics protection. By proper control of the temporal delay between the prepulse and the FSP pulse, optimal conditions were established for the generation of an electron beam with a divergence below 0.1 rad, detected energy up to 25 MeV, and a typical charge of 0.15 nC, reaching from 0.18 up to a maximum of 0.25 nC in ∼15% of the shots at a laser repetition rate of 10 Hz in the energy range above 1 MeV. The conversion of laser energy to bunch charge is 3.8 nC/J (>1 MeV). Numerical calculations supported the experimental findings and indicated the complex effect of acceleration mechanism related to DLA and SM-LWFA in a bell-shaped plasma profile. The approach of electrons trapping and acceleration in prepulse-induced plasma is versatile since it may be realized with different types of thin targets. However, liquid targetry is distinguished by its robustness, simplicity, and long-term operation in vacuum conditions, scalable to high repetition rate.

ACKNOWLEDGMENTS

The study was carried out within the framework of the scientific program of the National Center for Physics and Mathematics (project "Physics of High Energy Densities. Stage 2023–2025") with the use of equipment purchased under support of National project Science and Universities of Ministry of Science and Higher Education of the Russian Federation.

DATA AVAILABILITY

The data that support the findings of this article are not publicly available. The data are available from the authors upon reasonable request.

[1] T. Tajima and J. M. Dawson, Laser electron accelerator, Phys. Rev. Lett. **43**, 267 (1979).
[2] A. Pukhov, Z.-M. Sheng, and J. Meyer-ter-Vehn, Particle acceleration in relativistic laser channels, Phys. Plasmas **6**, 2847 (1999).
[3] V. Malka, Electron acceleration by a wake field forced by an intense ultrashort laser pulse, Science **298**, 1596 (2002).
[4] A. E. Hussein, Towards the optimisation of direct laser acceleration, New J. Phys. **23**, 023031 (2021).

[5] T. Wang, V. Khudik, A. Arefiev, and G. Shvets, Direct laser acceleration of electrons in the plasma bubble by tightly focused laser pulses, Phys. Plasmas **26**, 083101 (2019).

[6] C. Aniculaesei, The acceleration of a high-charge electron bunch to 10 GeV in a 10-cm nanoparticle-assisted wakefield accelerator, Matter Radiat. Extrem. **9**, 014001 (2024).

[7] O. N. Rosmej, High-current laser-driven beams of relativistic electrons for high energy density research, Plasma Phys. Control. Fusion **62**, 115024 (2020).

[8] K. Nakajima, Laser-driven electron beam and radiation sources for basic, medical and industrial sciences, Proc. Japan Acad. Ser. B **91**, 223 (2015).

[9] H. T. Kim and D. Margarone, Laser-driven accelerators, radiations, and their applications, Appl. Sci. **12**, 3662 (2022).

[10] S. Toth, SYLOS lasers: The frontier of few-cycle, multi-TW, kHz lasers for ultrafast applications at extreme light infrastructure attosecond light pulse source, J. Phys. Photonics **2**, 045003 (2020).

[11] M. Ouillé, Relativistic-intensity near-single-cycle light waveforms at kHz repetition rate, Light Sci. Appl. **9**, 47 (2020).

[12] C. G. R. Geddes, K. Nakamura, G. R. Plateau, C. Toth, E. Cormier-Michel, E. Esarey, C. B. Schroeder, J. R. Cary, and W. P. Leemans, Plasma-density-gradient injection of low absolute-momentum-spread electron bunches, Phys. Rev. Lett. **100**, 215004 (2008).

[13] A. Buck, Shock-front injector for high-quality laser-plasma acceleration, Phys. Rev. Lett. **110**, 185006 (2013).

[14] C. McGuffey, Ionization induced trapping in a laser wakefield accelerator, Phys. Rev. Lett. **104**, 025004 (2010).

[15] A. Pak, K. A. Marsh, S. F. Martins, W. Lu, W. B. Mori, and C. Joshi, Injection and trapping of tunnel-ionized electrons into laser-produced wakes, Phys. Rev. Lett. **104**, 025003 (2010).

[16] L. Rovige, Demonstration of stable long-term operation of a kilohertz laser-plasma accelerator, Phys. Rev. Accel. Beams **23**, 093401 (2020).

[17] J. Krall, A. Ting, E. Esarey, and P. Sprangle, Enhanced acceleration in a self-modulated-laser wake-field accelerator, Phys. Rev. E **48**, 2157 (1993).

[18] D. Hazra, A. Moorti, S. Mishra, A. Upadhyay, and J. A. Chakera, Direct laser acceleration of electrons in a high-Z gas target and the effect of threshold plasma density on electron beam generation, Plasma Phys. Control. Fusion **61**, 125016 (2019).

[19] R. Babjak, B. Martinez, M. Krus, and M. Vranic, Direct laser acceleration in varying plasma density profiles, New J. Phys. **26**, 093002 (2024).

[20] K. G. Miller, J. P. Palastro, J. L. Shaw, F. Li, F. S. Tsung, V. K. Decyk, C. Joshi, and W. B. Mori, Accurate simulation of direct laser acceleration in a laser wakefield accelerator, Phys. Plasmas **30**, 073902 (2023).

[21] P. M. King, Predominant contribution of direct laser acceleration to high-energy electron spectra in a low-density self-modulated laser wakefield accelerator, Phys. Rev. Accel. Beams **24**, 011302 (2021).

[22] L. M. Chen, Bright betatron X-ray radiation from a laser-driven-clustering gas target, Sci. Rep. **3**, 2013 (1912).

[23] P. Koester, G. C. Bussolino, G. Cristoforetti, A. Faenov, A. Giulietti, D. Giulietti, L. Labate, T. Levato, T. Pikuz, and L. A. Gizzi, High-charge divergent electron beam generation from high-intensity laser interaction with a gas-cluster target, Laser Part. Beams **33**, 331 (2015).

[24] M. M. Nazarov, T. A. Semenov, A. A. Tausenev, M. V. Chaschin, P. A. Shcheglov, A. V. Lazarev, D. A. Sidorov-Biryukov, A. V. Mitrofanov, V. M. Gordienko, and V. Y. Panchenko (Electron acceleration in nitrogen clusters by terawatt femtosecond laser, JETP Lett. **120**, 470 (2024).

[25] Y. Fukuda, Ultrarelativistic electron generation during the intense, ultrashort laser pulse interaction with clusters, Phys. Lett. A **363**, 130 (2007).

[26] Y. Ma, Ultrahigh-charge electron beams from laser-irradiated solid surface, Proc. Natl. Acad. Sci. U.S.A.**115**, 6980 (2018).

[27] N. Zaïm, F. Böhle, M. Bocoum, A. Vernier, S. Haessler, X. Davoine, L. Videau, J. Faure, and R. Lopez-Martens, Few-cycle laser wakefield acceleration on solid targets with controlled plasma scale length, Phys. Plasmas **26**, 033112 (2019).

[28] S. Feister, Relativistic electron acceleration by mJ-class kHz lasers normally incident on liquid targets, Opt. Express **25**, 18736 (2017).

[29] A. Mondal, Shaped liquid drops generate MeV temperature electron beams with millijoule class laser, Commun. Phys. **7**, 85 (2024).

[30] K. A. Ivanov, S. A. Shulyapov, I. N. Tsymbalov, I. P. Tsygvintsev, I. Y. Vichev, M. S. Krivokorytov, R. V. Volkov, and A. B. Savel'ev, Optically shaped mass-limited liquid sheet target for high repetition rate laser-driven acceleration, Phys. Plasmas **32**, 080702 (2025).

[31] K. A. Ivanov, D. A. Gorlova, I. N. Tsymbalov, I. P. Tsygvintsev, S. A. Shulyapov, R. V. Volkov, and A. B. Savel'ev, Laser-driven pointed acceleration of electrons with preformed plasma lens, Phys. Rev. Accel. Beams **27**, 051301 (2024).

[32] K. A. Ivanov, S. A. Shulyapov, D. A. Gorlova, I. P. Tsygvintsev, M. S. Krivokorytov, I. N. Tsymbalov, R. V. Volkov, and A. B. Savelev, Laser-accelerated MeV-scale collimated electron bunch from a near-critical plasma of a liquid jet target, Laser Phys. Lett. **21**, 075402 (2024).

[33] P. W. Bradford, Laser interactions with gas jets: electromagnetic pulse emission and nozzle damage, High Power Laser Sci. Eng. **12**, e98 (2024).

[34] M. Füle, A. P. Kovács, T. Gilinger, M. Karnok, P. Gaál, S. Figul, G. Marowsky, and K. Osvay, Development of an ultrathin liquid sheet target for laser ion acceleration at high repetition rates in the kilohertz range, High Power Laser Sci. Eng. **12**, e37 (2024).

[35] D. A. Gorlova, A. Y. Zavorotny, I. N. Tsymbalov, K. A. Ivanov, S. A. Shulyapov, R. V. Volkov, and A. B. Savel'ev, Neutron source from (γ,n) reactions at a laser-plasma accelerator and its use for electron beam characterization, J. Surf. Investig. X-Ray, Synchrotron Neutron Tech. **17**, 865 (2023).

[36] F. Salehi, M. Le, L. Railing, M. Kolesik, and H M. Milchberg, Laser-accelerated, low-divergence 15-MeV quasimonoenergetic electron bunches at 1 kHz, Phys. Rev. X **11**, 021055 (2021).

[37] V. A. Flegentov, K. V. Safronov, S. A. Gorokhov, A. S. Tishchenko, S. F. Kovaleva, A. V. Potapov, and A. V. Pavlenko, Pulsed laser-plasma gamma radiation source for radiography, Quantum Electron. **51**, 866 (2021).

[38] J. Feng, Laser plasma-accelerated Ultra-intense electron beam for efficiently exciting nuclear isomers, Laser Photon. Rev. **17**, 2300514 (2023).

[39] J. L. Shaw, Microcoulomb $(0.7 + 0.4 - 0.2\ \mu C)$ laser plasma accelerator on OMEGA EP, Sci. Rep. **11**, 7498 (2021).

[40] Y. F. Li, Electron beam and betatron x-ray generation in a hybrid electron accelerator driven by high intensity picosecond laser pulses, High Energy Density Phys. **37**, 100859 (2020).

[41] M. Mirzaie, N. A. M. Hafz, S. Li, K. Gao, G. Li, Q. Ul Ain, and J. Zhang, Laser acceleration in argon clusters and gas media, Plasma Phys. Control. Fusion **58**, 034014 (2016).

[42] S. Li, Ultrafast multi-MeV gamma-ray beam produced by laser-accelerated electrons, Phys. Plasmas **24**, 093104 (2017).

[43] A. Y. Krukovskiy, V. G. Novikov, and I. P. Tsygvintsev, 3D simulation of the impact made by a noncentral laser pulse on a spherical tin target, Math. Model. Comput. Simulations **9**, 48 (2017).

[44] S. Faik, A. Tauschwitz, and I. Iosilevskiy, The equation of state package FEOS for high energy density matter, Comput. Phys. Commun. **227**, 117 (2018).

[45] I. Y. Vichev, A. D. Solomyannaya, A. S. Grushin, and D. A. Kim, On certain aspects of the THERMOS toolkit for modeling experiments, High Energy Density Phys. **33**, 100713 (2019).

[46] J. Derouillat, Smilei : a collaborative, open-source, multi-purpose particle-in-cell code for plasma simulation, Comput. Phys. Commun. **222**, 351 (2018).

[47] A. Pukhov and J. Meyer-ter-Vehn, Laser wake field acceleration: the highly non-linear broken-wave regime, Appl. Phys. B Lasers Opt. **74**, 355 (2002).

[48] I. Tsymbalov, D. Gorlova, K. Ivanov, E. Starodubtseva, R. Volkov, I. Tsygvintsev, Y. Kochetkov, P. Korneev, A. Polonski, and A. Savel'ev, All-optical blast-wave control of laser Wakefield acceleration in a near-critical plasma, Phys. Rev. Lett. **134**, 025101 (2025).